Contents lists available at ScienceDirect

Composites Part A

Investigation of power and amplitude control in continuous ultrasonic welding of unidirectional CFRPs: A comparative study

Maximilian Janek ⓘ *, Dominik Görick, Lars Larsen, Stefan Jarka, Michael Kupke

German Aerospace Center (DLR), Am Technologiezentrum 4, Augsburg, 86159, Germany

ARTICLE INFO

ABSTRACT

The presented study aims to evaluate two different control methods for continuous ultrasonic welding of carbon fibre reinforced high performance polymers. A novel power-control mechanism is compared with a state-of-the-art amplitude-controller. Both control methods are applied to a carbon composite material with a LowMelt-PolyArylEtherKetone (LM-PAEK) thermoplastic matrix and evaluated for three different fibre layups of the composite material. The controllers are evaluated based on in-situ data, mechanical properties of the weld seam and its quality ensured by non-destructive testing and microscopic analyses. The similarities and differences between the controllers are discussed and formulated in detail.

1. Introduction

The aerospace industry has been undergoing a notable shift in materials science, with growing interest for Thermoplastic Composites (TPCs) for structural applications in aircraft over the past few years. This trend is driven by a multitude of technological advancements and evolving market demands that emphasize the need for lighter, stronger, and more sustainable aircraft. Thermoplastic composites stand out as an ideal choice for aircraft structures due to several compelling advantages [1]. Furthermore, TPCs offer significant advantages in automation and production rate capabilities compared to traditional thermoset composites, enabling high-volume production and paving the way for future automation applications in industries such as aerospace, automotive, and energy. Their lightweight nature significantly enhances fuel efficiency and reduces operating costs. Moreover, these materials exhibit exceptional fatigue resistance, making them well-suited for components that undergo cyclic loading. The processability of thermoplastic materials allows for efficient manufacturing methods, such as thermoforming, injection molding, and compression molding, enabling the creation of intricate shapes and structures. The ability to repair thermoplastic composites easily is a significant asset, saving both time and resources during maintenance. Additionally, their impact resistance and durability make them more resilient to environmental factors like bird strikes, hail, and extreme temperatures. The design flexibility of thermoplastic composites facilitates innovative and efficient aircraft designs, potentially reducing the need for numerous fasteners and joints. A further important advantage is the ability to weld thermoplastic

composites which is a significant advantage for assembly processes. Welding allows for the creation of seamless joints and the elimination of mechanical fasteners, which can introduce stress concentrations and potential failure points. This capability simplifies the assembly process, reduces the number of components, and improves the overall structural integrity of the aircraft [1].

In recent years, various welding processes, such as resistance, induction, laser and ultrasonic welding [1–3], have been investigated in science and some are already being used in the aerospace industry for industrialized products as for example the leading edges for Airbus A340 made of Polyphenylensulfid (PPS) [4] or the brackets of an Airbus A350 [5] made of Polyetheretherketon (PEEK).

The ultrasonic welding process described in this study, which was initially limited to static spot welding applications for an extended period, has recently experienced a surge in adoption for continuous processing, thereby expanding its scope and versatility in industrial manufacturing settings [6–9]. The first applications of robot-based continuous ultrasonic welding were successfully demonstrated at German Aerospace Center (DLR) Center for Lightweight Production Technology (ZLP) Augsburg back in 2018.[1] Some of the first applications were the welding of PEEK omega stringers onto an oven vacuum-consolidated skin or of press-consolidated PPS segments of a pressure bulkhead [10]. These examples impressively demonstrated that ultrasonic welding technology can be utilized on a robot for continuous weld seams [11]. At that point in the development process, specifically during the initial trials, strength values of 23.3 MPa with a

---

standard deviation of 1.6 MPa could be achieved for PPS considering the theoretically attainable bonding area (12.7 mm by 25.4 mm) at the interface between the mating weld partners in the assessment of joining strength [10]. The single lap strength was thus not scaled to the actual joined surface in case of partial welding.

The Multifunctional Fuselage Demonstrator (MFFD) project was the first project ever to demonstrate the use of the robot-based CUW process for a full-scale application in an industrial scale. In the project, a thermoplastic airplane barrel with a length of 8 m and a diameter of 4 m was manufactured. The Z-shaped 8 m long stringers within the upper-shell were integrated by robot-based CUW by the DLR ZLP Augsburg [12].[2]

In the meantime, the robotic CUW is also being studied by various research institutes and companies using end-effectors with a very similar design [13]. In this context, there have also been numerous publications in recent years that shed light on various aspects of the process [14,15], such as energy director design and influence [16, 17], process parameters [18], tilting of the sonotrode of the end-effector [13] in order to characterize and evaluate these variables and clamping influences [6,19]. However, all these approaches have in common that the parameters are often supposedly optimized for a material set, but ultimately do not produce consistent quality over the entire weld seam length. Furthermore, these tests are often only carried out on a laboratory scale on flat weld adherends with ideal conditions [13]. However, this does not reflect the requirements of an industrial process in which components are to be welded at full-scale [20]. In such scenarios, there are always irregularities in the components and in the conditions, such as the clamping and alignment of the parts, which can have a significant influence on the welding process [19]. Real-Time control of the welding process is therefore a decisive step in industrialization.

The close correlation between specific process data and parameters, as identified by Benatar and Gutowski [21–23], as well as the initial in-situ monitoring conducted by Villegas [18] for static ultrasonic welding, is not yet reflected in published works concerning various methodologies for the control of continuous ultrasonic welding.

Previous studies on static and continuous ultrasonic welding have investigated various process parameters as direct control variables or as indirect control signals [9]. For static ultrasonic welding in particular, parameters such as the welding energy and the resulting displacement of the sonotrode were measured in order to monitor and indirectly control the process [24]. For this purpose, a defined value was set as a termination criterion [24]. Villegas contributed to the fundamental understanding of the relationship between weld power, sonotrode displacement and strength development of the weld seam, by closely monitoring the process [18]. Further investigations took the travel speed and sonotrode force into account as additional process steering parameters [7]. In the field of static ultrasonic welding, initial investigations were also carried out into the effects of morphological properties such as crystallinity and their active contribution as a process steering parameter [25].

In terms of continuous ultrasonic welding, which is guided on a linear axis [26] or by a robot [13], fewer investigations have been carried out to date. The state of the art is the control of the peak-to-peak amplitude, while certain process variables, such as the process speed or process forces, are varied as steering variables [13,26–28].

The presented study focuses on the active control of the continuous ultrasonic welding process to analyse the influence of the two control variables, the peak-to-peak amplitude and the welding power. While previous studies have focused on optimizing the control variables to produce the best possible weld [13,26], this study aims to provide a clear understanding of the controller architecture. Therefore, a predetermined set of process parameters is defined, which is then applied to three different materials using both controller architectures.

Consequently, this study presents a novel approach to a power-control method, which is compared to the prevailing state-of-the-art amplitude-controller.

2. CUW at DLR ZLP

The DLR is equipped with two functionally redundant ultrasonic welding end-effectors, one of which is integrated with a robotic system for scaled-up demonstrator fabrication, while the other is mounted on a linear axis for controlled bench testing and fundamental research purposes. This dual setup enables the sequential implementation of a 'bench-to-production' workflow, wherein novel methodologies can be developed, tested, and refined in a controlled environment prior to being directly translated to the robotic welding process, thereby facilitating a streamlined transition of research findings to real-world applications. The presented study is making use of the linear axis application as shown in Fig. 1 in order to reduce boundary conditions and side effects due to the robot stiffness [29]. Both end-effectors are equipped with three main components as showcased in Fig. 1, a *Compaction Roller (1)*, a stack of *Converter*, *Booster* and *Sonotrode (2)* as well as the *Compaction Unit (3)*.

Furthermore, a modular aluminium anvil (Fig. 1(right)) is mounted to the bench to align the weld setup of the adherends, as described in Section 3.1 accordingly. Compared to other anvils and clamping systems described in the literature [15], a selective clamping system with two discrete positions (4) and (5) is used instead of a linear, continuous clamping system. A key reason for this approach is that the final application on real component geometry cannot guarantee full-field clamping, as this results in an immensely high and expensive use of operating resources such as molds and jigs [20]. The control system and subcomponents are mainly developed by DLR and are operated by a *TwinCAT*® based Programmable Logic Controller (PLC). However, the centerpiece namely the ultrasonic welding machine is an off the shelve equipment provided by *Branson Ultrasonics Corp.*®. The system used is powered by a *DCXs20VRT Power Supply* and equipped with a 20 kHz converter, a titanium booster (500/900 Series-gold) with a gain of 1:1.5 and a flat surface sonotrode with an area of 13 mm × 25 mm. The maximum peak-to-peak amplitude of this setup is given at 100 μm, which is defined as 100% in this study hereafter.

Power-Controller:

This study presents a novel control loop, developed by the authors, which uses the actual monitored amplitude of the generator to control the power output. Hence, the operator provides a certain power level as desired value through the PLC that is processed and sent back to the welding device as a magnitude of amplitude. The control loop is realized by a Proportional Integral Derivative (PID) controller.

Amplitude-Controller:

The manufacturers amplitude-controller was used in comparison. Although the closed system cannot be described in more detail due to a lack of insight, it can be assumed from the manufacturer's specifications [30] and corresponding technical literature [31] that the controller architecture performs cascaded control of the piezoelectric actuators, which is based on current and voltage measurements [30–32]. Furthermore, a digital input is provided that enables external control of the amplitude [30]. This parameter is utilized to send the foreseen amplitude from the PLC to the power supply of the welding device. This arrangement allows to control the amplitude at a certain level with a desired value provided by the operator via the PLC, while the power is monitored.

3. Experimental procedures

3.1. Materials and weld preparation

The study has been executed with a carbon composite material provided by *Toray*®. Their *TC1225* material consists of carbon fibres and a
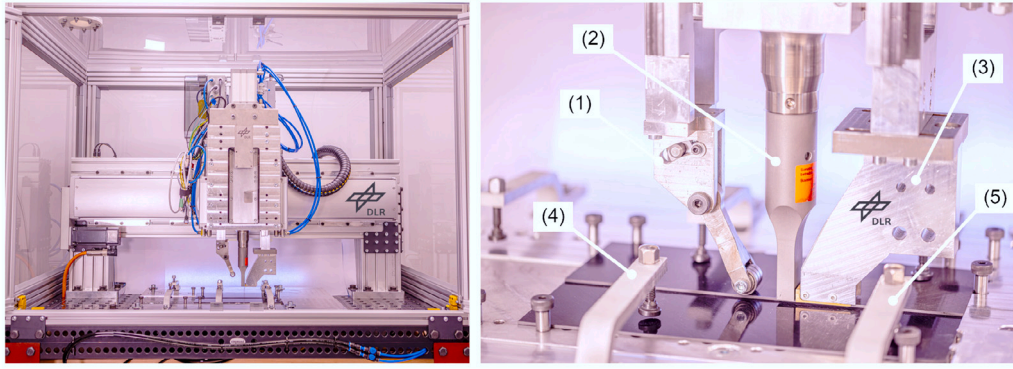

Fig. 1. Continuous ultrasonic welding bench (left), welding setup on modular anvil (right).
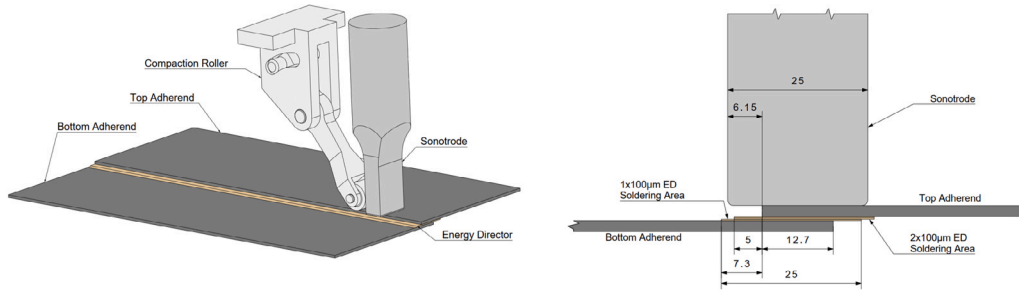

Fig. 2. Welding setup and ED arrangement shown without compaction unit in isometric view (left), detailed side view (right) - not to scale, dimensions in mm.

thermoplastic, semi-crystalline LM-PAEK polymer matrix that provides advanced mechanical properties and suitable processability for welding applications, provided by its viscosity and processing temperature characteristics [33].

The material has been supplied as pressconsolidated large format sheets (1200 mm × 2500 mm) made from unidirectional (UD) tape. These sheets have been water jet cut to the size of 296 mm × 104.6 mm in order to prepare the welding partners.

Three different stacking sequences of this material have been used to evaluate the effects of the power- and amplitude-controller for the ultrasonic welding process. Two stacks have 14 layers, such as $[(0, 90)_3 0]_s$ and $[45, 90, 135, 0, 45, 135, 0]_s$. The third contributed a pure UD stacking of $[0]_{12}$. Each layer measures a ply thickness of 0.14 mm, resulting in 1.96 mm for the 14 layers and 1.68 mm for the 12 layers material.

Furthermore, a so called Energy Director (ED) [1] has been prepared for the welding and arranged between the top and bottom adherend of the welding setup, as shown in Fig. 2. This ED equally made from LM-PAEK (APTIV AE™ Film, 6013-AEG-100, 100 μm) is supplied as a neat resin film with a thickness of 100 μm. Three ED layers are used for this study, two layers fastened to the top adherend, one to the bottom adherend, see Fig. 2. The primary focus of this study is to investigate the influence of the controllers, thus the effects of the ED were not further explored. However, for a comprehensive understanding of the system, future research should examine the secondary effects of various ED (co-consolidation, structuring, crystallinity, material), as previously investigated by Villegas et al. [34] and Tsiangou et al. [35,36]. The bottom and top adherend of the three material stacks are arranged in an overlap configuration of 12.7 mm as shown in Fig. 2. Each part of the setup is thoroughly cleaned using isopropyl alcohol. The ED is preliminary fastened to the bottom and top adherend using a soldering iron. Securement of the assembly was achieved through the application of five discrete fixation points, strategically located external to the weld interface, thereby providing a stable and rigid attachment while avoiding interference with the ultrasonic welding process.

To improve readability, the layer stacking $[(0, 90)_3 0]_s$ is referred to below as material #01 or MAT01, the quasi isotropic stacking $[45, 90, 135, 0, 45, 135, 0]_s$ as material #02 or MAT02 and the unidirectional stack $[0]_{12}$ as material #03 or MAT03. Furthermore, for materials #01 and #03, the 0° top layers of the upper and lower adherends were oriented perpendicular to the welding direction, hence creating a 90° angle between the fiber orientation and the weld line. In contrast, material #02 exhibited a 45° angle between the top layers of the upper and lower adherends and the welding direction, with the fibers oriented orthogonally to each other, resulting in a herringbone-like pattern in the weld line.

3.2. Process parameter and approach

In order to reduce boundary conditions, a constant and overall process parameter setup is defined. These settings were chosen for material #01 by a current feasible and iterative method and were then applied to material #02 and #03 without further adaptation. This approach provides insight into the differences of the power- and amplitude-controller and their effects on the diverse layer stacks, although it can be assumed that this approach may not produce the best results for all of the materials.

Since the upheaval of this publication is a power-controller for the ultrasonic welding process, this controller is initially used to iterate the process parameters. Subsequently, the monitored amplitude during the power-controlled process is averaged to define a comparable setup for the amplitude-controlled welding. Based on this, the following settings were made for the power-controlled continuous welding process and its main components as described by Larsen et al. [1].

A compaction roller force F_R=300 N, a sonotrode force F_S=800 N, a compaction unit pressure of p_{CU}=16 bar as well as a welding velocity of V_w=15 mm/s have been chosen. The supposedly optimized welding power was set to P_w=1025 W.

Five welds were made with each material using the power-control mechanism. The measured amplitudes have been averaged along each welding to $\overline{A}_w$ and eventually averaged over the five welds to a total
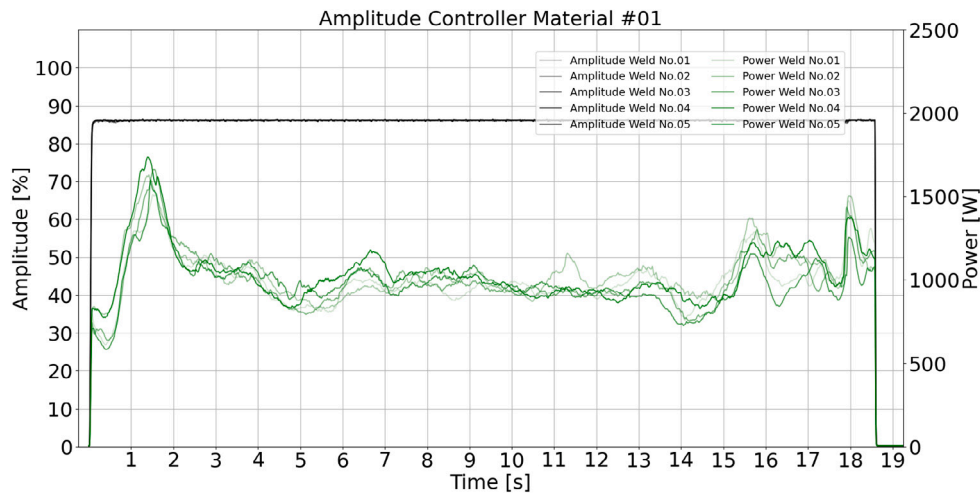
Fig. 3. Amplitude and power curves of the amplitude-controller for material #01.

average amplitude $\overline{A}_W$ (see Table 1). This procedure is applied to each material to define an individual averaged amplitude setting for the five amplitude-controlled welds which are compared afterwards. A similar averaging is applied to the actually monitored power, as the custom power-controller deviates from set power default. The averaged power for each individual weld is represented by $\overline{P}_W$ (see Table 1).

4. Power and amplitude data

The diagrams hereafter, Figs. 3–8, show the amplitude and power curves for the individual material and the respective controller. The amplitude values are depicted in black, while the power data are represented in green, with both curves rendered in a faded tone to distinguish between the five individual welds. Figs. 3, 5 and 7 show a stable and constant amplitude attitude with a deviation of $\pm0.5\%$ as an absolute value. On the other hand the power-controlled welds are affected by a control deviation of ±50 W in power, that represents a relative divergence of $\pm4.88\%$. As previously mentioned, this study does not focus on the optimization of the power-controller, which is why a control error of less than 5.0% is accepted.

A comparative analysis of the two controllers, conducted across the three distinct materials, reveals that disparate curves are produced for each controller when paired with the same material and identical control parameters, suggesting an offset and calibration issue. Although the curves exhibit some degree of variability, each controller yields analogous trends and curve morphologies across the five replicate welds, indicating a consistent response.

Upon comparing the macroscopic trends of the curves across the three different materials, it is evident that both the amplitude and power exhibit a high degree of consistency within the established weld seam region for material #03 for both controllers, (see Figs. 7 and 8). In contrast, a notable inversion of the amplitude and power curve is observed for materials #01 and #02 when their respective diagrams are superimposed, revealing a distinct characteristic response for these materials. Specifically, Fig. 3 illustrates a global maximum in power occurring within the time interval of 1–2 s, which corresponds to a concurrent global minimum in amplitude, as depicted in Fig. 4. Additionally, a notable variation in power is evident within the 14–16 s time interval in Fig. 3, which is concurrently mirrored by a corresponding change in amplitude within the same interval in Fig. 4. A similar pattern of behaviour is observed, albeit in a less pronounced manner, for material #02 in Figs. 5 and 6.

A direct correlation between vibration amplitude and dissipated energy has been empirically established by Benatar and Gutowski [23] in the context of static ultrasonic welding of composite materials,

and further elucidated by Villegas [18]. This established relationship corroborates the notion that a direct comparison of controllers reveals a plausible interaction between these two variables as previously described.

A cross-material analysis of the power curves for amplitude-controlled welds reveals a distinct trend in the established weld seam within the 2–15 s time frame. Specifically, material #01 and #02 exhibit a decrease in power of about $\approx 10\%$ for material #01 and $\approx 20\%$ for material #02, whereas material #03 displays a slight increase in power $\approx 10\%$, suggesting a material and temperature dependent variation in the viscoelastic heat dissipation and damping. The interactive relationship between amplitude and power reveals an inverse behaviour in the power-controlled welds, as evidenced by the amplitude curves. Notably, material #01 and #02 exhibit a monotonic increase in amplitude, whereas material #03 displays a plateau-like behaviour, with the amplitude remaining relatively constant.

The characteristics exhibited by the amplitude and power curves are subjected to a more detailed analysis in Section 7, where their behaviour is interpreted in the context of the study's overall outcomes.

5. Weld strength evaluation

A commonly used method for determining the strength of the welded joint in the field of static and continuous ultrasonic welding is the ascertainment of the Lap Shear Strength (LSS) [1,8,37–39]. Test specimens with the dimensions of 25.4 mm in width and 190.5 mm in length are water jet cut from the welded adherends. Considering the overlap of 12.7 mm, a length of 101.6 mm is guaranteed for both the upper and lower adherend as shown in Fig. 9. Consequently, ten Single Lap Shear (SLS) specimen were fabricated from each weld, taking geometric boundary conditions such as blend and clamping area during waterjet cutting into account. The following evaluation refers to the individual sample numbers, that are ascending along the welding direction, see Figs. 9, 10, 11 and 12. The specimen geometry and the pulling test velocity of $1.3 \frac{\text{mm}}{\text{s}}$ have been chosen in accordance with ASTM D1002. Due to the lateral offset provided by the single overlap configuration, the specimen were clamped utilizing asymmetrical jaws in order to equalize the offset by positioning the weld seam concentric with the tensile test axis. Eventually, the monitored maximum tensile force F_m is considered in relation to the theoretical maximum bonding area of 12.7 mm $\times$ 25.4 mm, which leads to an actual LSS stated in [MPa]. This study does not consider an effective LSS value that merely takes the bonded area into account [19], as a true comparability between the two different process controllers is aimed at.
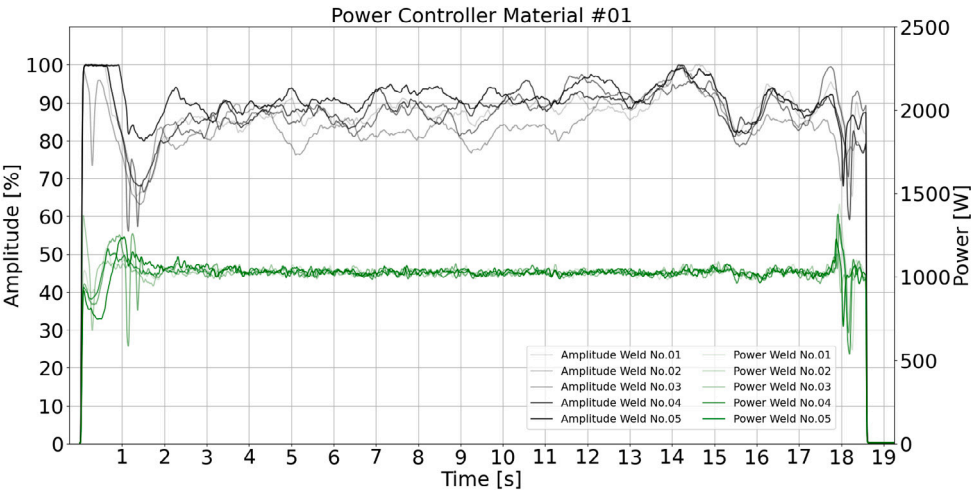
Fig. 4. Amplitude and power curves of the power-controller for material #01.
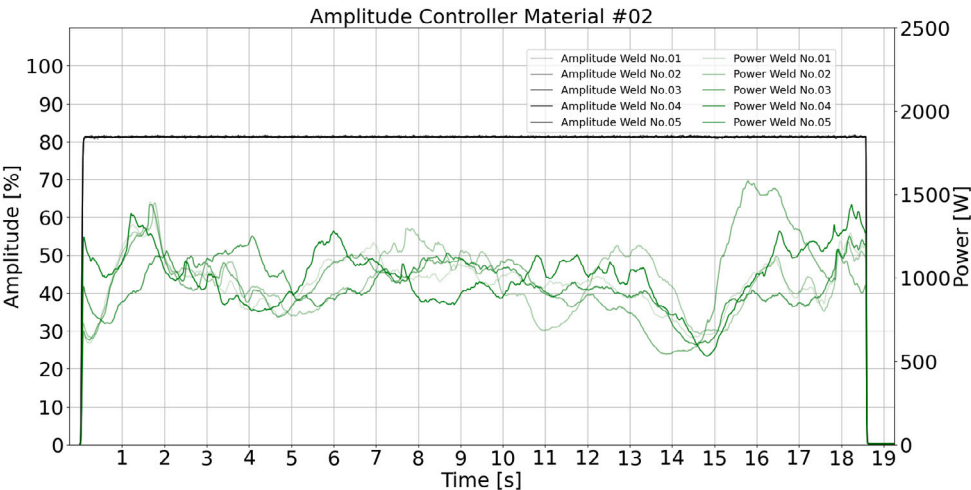

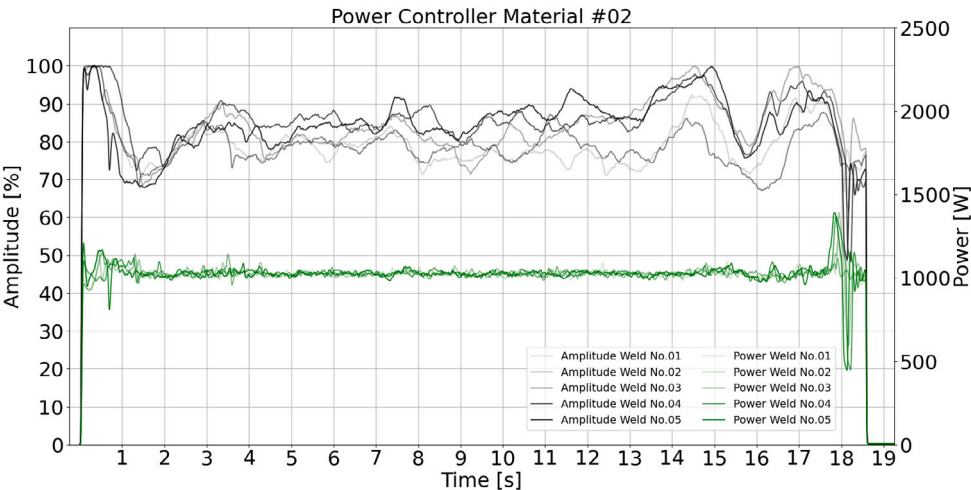**Fig. 5.** Amplitude and power curves of the amplitude-controller for material #02.

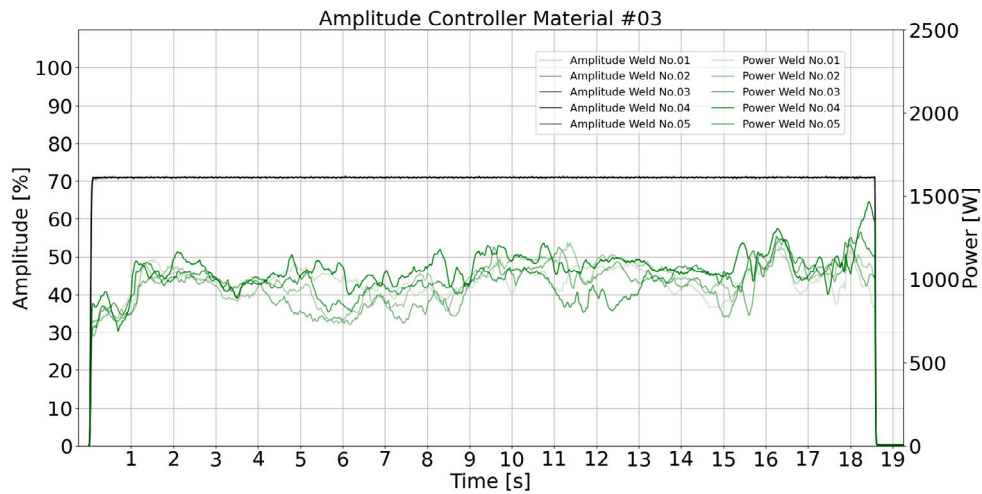**Fig. 6.** Amplitude and power curves of the power-controller for material #02.

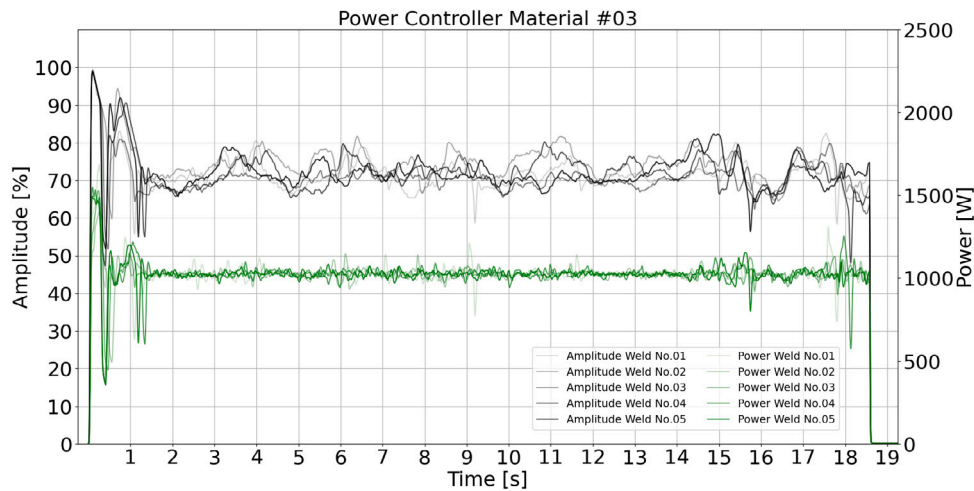**Fig. 7.** Amplitude and power curves of the amplitude-controller for material #03.

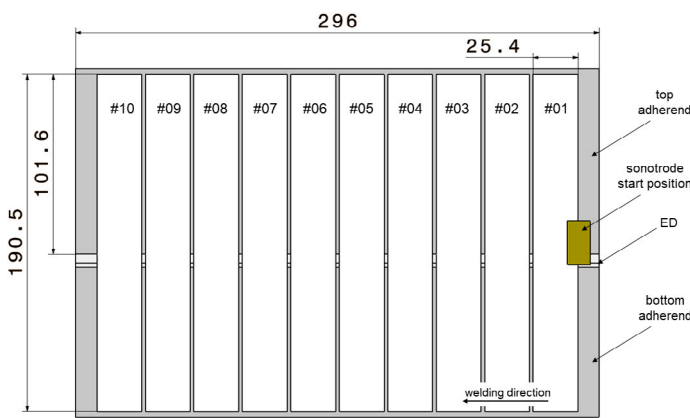**Fig. 8.** Amplitude and power curves of the power-controller for material #03.

Fig. 9. SLS coupon arrangement across top and bottom adherend weld configuration.

Four of the five welds of each material and each control method are processed into SLS coupons, while the fifth is utilized for microscopic imagery. Therefore, a total of 240 SLS samples are evaluated.

The first bond strength evaluation is carried out with the focus on the individual samples along the weld seam, comparing the amplitude and power-controller within a material and conclusively beyond the

three materials. Each figure (Figs. 10–12.) presents the mean LSS sample value averaged between the four welds for the individual material and specific control mechanism, as well as the minimum to maximum range of the LSS values at a certain sample position.

Material #01

Comparing the sample LSS values between the power- and amplitude-controller for the material #01 a notable difference is marked by the minimum to maximum range especially for the sample numbers #02 to #06, while sample number #01 and #07–#10 behave quite similar in their absolute maximum value and spread to each other. Moreover, the remarkable drop between sample number #08 and #09 appear for both controllers. While the LSS tend to raise from the start up to sample number #08 for the power-controlled welds, a robust plateau with fairly high values establish for the amplitude-controller in the same interval. However, peak values above 40 MPa are gained for both approaches of process control, see Fig. 10 and Table 2.

Material #02:

Applying the power-controller to the material #02 evokes a similar trend in LSS values as for material #01. A mid range start value between 15–20 MPa rises up to 35 MPa at sample number #08, followed by a drop of the mean value to ≈15 MPa, recovered by sample number #10 at ≈27 MPa close to the mean value of sample number #08. In comparison, the amplitude-controller does not behave in the same manner as for material #01. Merely a reasonable low start value, as well as a drop by sample number #09 can be perceived as a common

Table 1
Average power & amplitude.

Material	Controller POW/AMP	Weld No. [–]	P_w [W]	$\overline{P}_w$ [W]	$\overline{P}_W$ [W]	A_w [%]	$\overline{A}_w$ [%]	$\overline{A}_W$ [%]
MAT01	POW	01	1025.0	1009.8	–	–	–	86.2
MAT01	POW	02	1025.0	1010.2	–	–	–	82.6
MAT01	POW	03	1025.0	1009.8	–	–	–	86.2
MAT01	POW	04	1025.0	1010.0	–	–	–	86.6
MAT01	POW	05	1025.0	1009.8	–	–	–	89.4
MAT01	POW	[01-05]	–	–	1009.9	–	–	86.2
MAT01	AMP	01	–	981.7	–	86.2	84.6	–
MAT01	AMP	02	–	1024.5	–	86.2	84.6	–
MAT01	AMP	03	–	988.0	–	86.2	84.7	–
MAT01	AMP	04	–	964.6	–	86.2	84.7	–
MAT01	AMP	05	–	1022	–	86.2	84.7	–
MAT01	AMP	[01-05]	–	–	996.2	–	–	84.7
MAT02	POW	01	1025.0	1010.1	–	–	–	78.0
MAT02	POW	02	1025.0	1010.1	–	–	–	83.0
MAT02	POW	03	1025.0	1009.9	–	–	–	77.6
MAT02	POW	04	1025.0	1010.4	–	–	–	84.5
MAT02	POW	05	1025.0	1010.0	–	–	–	83.2
MAT02	POW	[01-05]	–	–	1010.0	–	–	83.2
MAT02	AMP	01	–	954.7	–	83.2	79.8	–
MAT02	AMP	02	–	962.7	–	83.2	79.9	–
MAT02	AMP	03	–	983.0	–	83.2	79.8	–
MAT02	AMP	04	–	939.7	–	83.2	79.8	–
MAT02	AMP	05	–	990.2	–	83.2	79.8	–
MAT02	AMP	[01-05]	–	–	966.1	–	–	79.8
MAT03	POW	01	1025.0	1010.3	–	–	–	70.3
MAT03	POW	02	1025.0	1010.0	–	–	–	73.2
MAT03	POW	03	1025.0	1010.3	–	–	–	69.6
MAT03	POW	04	1025.0	1009.8	–	–	–	70.9
MAT03	POW	05	1025.0	1009.7	–	–	–	71.2
MAT03	POW	[01-05]	–	–	1010.0	–	–	71.0
MAT03	AMP	01	–	969.3	–	71.0	69.8	–
MAT03	AMP	02	–	973.3	–	71.0	69.8	–
MAT03	AMP	03	–	936.9	–	71.0	69.8	–
MAT03	AMP	04	–	973.9	–	71.0	69.8	–
MAT03	AMP	05	–	1045.3	–	71.0	69.8	–
MAT03	AMP	[01-05]	–	–	979.7	–	–	69.8

behaviour. In comparison to the power-controller, it is noticeable that the deviation from the mean value is increased at sample #07 and #08, while the value at sample #10 is lower than at sample #08, respectively a recovery is not pronounced as much as within the power-controlled welds, see Fig. 11.

Material #03:

The analysis of the LSS of both power and amplitude-controller for material #03, shows that overall peak values are achieved with each method, while the minimum to maximum spread is narrowed, see Fig. 12 and Table 2. Particularly striking is the constant behaviour of the power-controlled welds along the entire seam length providing constant mean values greater than or equal to 35 MPa. A comparable robust behaviour can be seen for the amplitude-controlled welds with focus on sample number #09, that does not significantly drop as previously at material #01 and #02. However, the mean LSS at sample number #01 is recognizably lower than for the others within the amplitude-controlled welds but also a third lower than the lowest mean value of the power-controlled welds for material #03 (see Fig. 12).

Comparison across Material #01–#03:

Material #01 and material #02 show a significant drop of LSS between sample #08, #09 and #10. Furthermore, sample number #01 for all three materials seems to be lower compared to the average across the weld seam within the amplitude-controlled welds. Regardless of the control architecture, the three materials reflect different stages in weld and heat propagation [18] (see Section 7), that are depicted in the LSS by the absolute maximum values as well as the variance, represented by the minimum to maximum range across the weld seams. While material #02 delivers a largely diffuse field of LSS, material #01 delivers stable and high LSS values in the mid weld seam area, particularly by the amplitude-controller. Material #03 characterizes this even more precisely and delivers high, robust LSS values along the entire weld seam for both control methods.

Additionally to the evaluation of the LSS on individual sample positions, the analysis within an entire weld seam is performed to demonstrate the homogeneity of the weld quality. Therefore, Table 2 provides the mean LSS stated as $\overline{\sigma}_{\text{LSS}}$, the respective minimum and maximum values σ_{min} and σ_{max} as well as the consequent Sample Standard Deviation (SSD) as an absolute SSD_{abs} and relative SSD_{rel} dimension. The absolute SSD is calculated as mentioned in Eq. (1)., while the relative value is the according fraction to the mean value $\overline{\sigma}_{\text{LSS}}$. Notably, Figs. 10–12 illustrate the elongation of variation, as demarcated by the minimum and maximum values, for each specimen at discrete sample positions across the entirety of the welds. In contrast, the SSD quantifies the magnitude of dispersion, as indexed in Table 2 of a specimen's value relative to the mean within a singular weld.

$$SSD_{abs} = \sqrt{\frac{1}{N-1}\sum_{i=1}^{N}(\sigma_i - \overline{\sigma}_{LSS})^2} \tag{1}$$

Therefore, Table 2 unveils the potential of the ultrasonic welding process, represented by peak LSS values up to 48.4 MPa for the amplitude-controller and an extremely low standard deviation of less than 10% for the power-controlled welds of material #03.
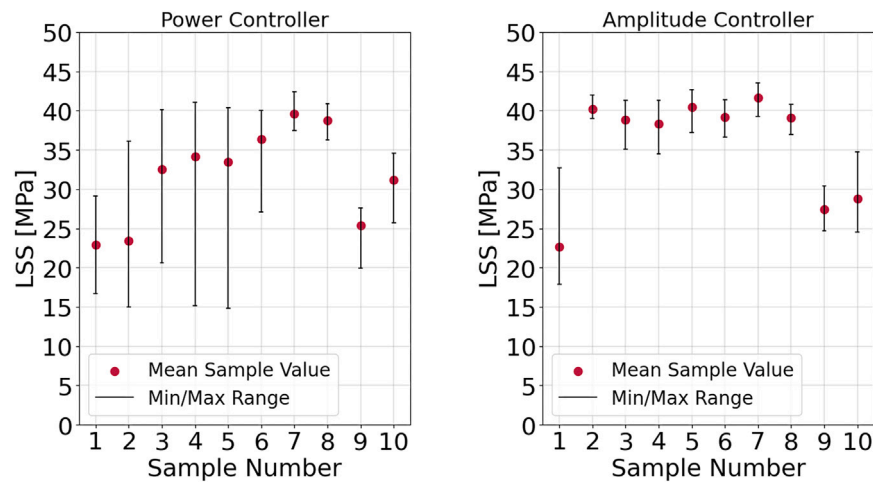
Fig. 10. Comparison of the LSS sample values for the Material #01 of the power- and amplitude-controller.
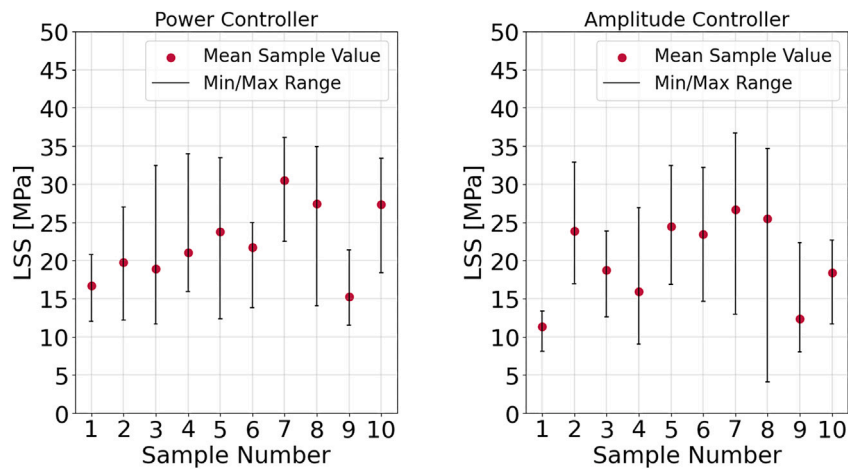

Fig. 11. Comparison of the LSS sample values for the Material #02 of the power- and amplitude-controller.
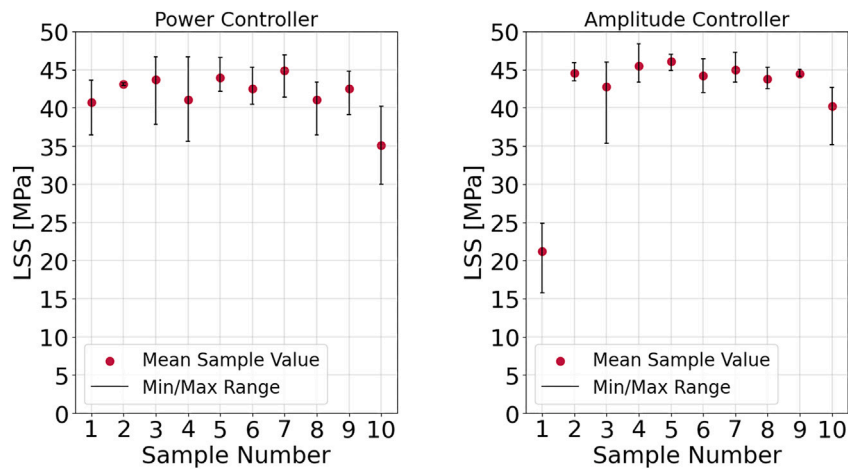

Fig. 12. Comparison of the LSS sample values for the Material #03 of the power- and amplitude-controller.

Table 2
LSS values overview including standard deviation - superior values highlighted in blue, inferior values denoted in yellow.

Material	Controller POW/AMP	Weld No. [–]	$\bar{\sigma}_{\mathrm{LSS}}$ [MPa]	$\sigma_{\min}$ [MPa]	$\sigma_{\max}$ [MPa]	SSD_{abs} [MPa]	SSD_{rel} [%]
MAT01	POW	01	36.6	27.3	41.0	4.72	12.9
MAT01	POW	02	23.8	14.8	42.4	9.80	41.1
MAT01	POW	03	33.4	15.7	41.1	7.44	22.3
MAT01	POW	04	33.4	17.6	40.2	7.03	21.0
MAT01	AMP	01	34.0	21.5	41.2	7.09	20.9
MAT01	AMP	02	38.0	29.4	43.5	4.25	11.2
MAT01	AMP	03	35.9	18.4	42.8	7.41	20.6
MAT01	AMP	04	34.9	17.9	41.4	7.93	22.8
MAT02	POW	01	22.5	11.6	30.3	5.59	24.8
MAT02	POW	02	23.7	12.0	36.1	8.65	36.4
MAT02	POW	03	14.7	11.5	22.5	3.29	22.3
MAT02	POW	04	28.1	16.5	34.0	6.18	22.0
MAT02	AMP	01	24.0	11.2	35.0	7.20	30.0
MAT02	AMP	02	20.2	8.1	32.5	7.30	36.1
MAT02	AMP	03	16.7	4.1	32.9	7.04	42.0
MAT02	AMP	04	19.3	8.0	36.7	10.89	56.5
MAT03	POW	01	42.3	35.6	46.7	3.52	8.3
MAT03	POW	02	39.8	30.0	43.7	3.91	9.8
MAT03	POW	03	43.6	32.1	46.7	4.10	9.4
MAT03	POW	04	41.8	37.8	46.9	2.61	6.3
MAT03	AMP	01	42.0	22.9	48.4	7.16	17.0
MAT03	AMP	02	40.8	21.3	46.1	7.05	17.3
MAT03	AMP	03	41.4	15.8	47.3	8.65	20.9
MAT03	AMP	04	43.0	24.9	46.9	6.23	14.5

The relative SSD is valuable to study the differences between material #01, #02 and #03. When aberration *MAT01-POW-02* (see Table 2) is excluded from the analysis, one can recognize the highest SSD for material #02, a moderate SSD for material #01 and the lowest SSD for material #03, regardless of the control methodology. This supports the previous assumption that the materials were in unlike stages [18] of the welding process, which is discussed in more detail in Section 7. When collating the $\sigma_{\min}$ and $\sigma_{\max}$ of each material between the controller methods, no significant difference can be found. However, the overall minimum and maximum values are issued by the amplitude-controller.

6. Weld seam inspection

The quality of the weld seams is to be compared and contrasted using three methods. Firstly, ultrasonic flaw detection is used to visualize the homogeneity of the weld seams. Subsequently, cross-sectional samples are taken at specific positions of the weld seam for evaluation using optical microscopy. As a concluding step, a post-test visual examination of the fracture surface is performed, facilitating a qualitative analysis of the specimen's failure mode and associated fracture characteristics.

6.1. Ultrasonic flaw detection

Ultrasonic flaw detection scans are recorded by utilizing an *OmniScan SX* device by *OLYMPUS®*, enabled by a *5L64-NW1* phased array probe and a *SNW1-OL-IHC* polyamid wedge. The welded top and bottom adherend were scanned as shown in Fig. 13 covering the weld seam width of 12.7 mm by the probes' field of view making use of water as the coupling medium. Cropping the C-scan data to the region of interest, i.e. exclusively the weld seam, enables a targeted evaluation of the weld seam quality, as shown in Table 3.

In accordance with the AITM6-4010 standard [40], the attenuation of the ultrasound signal by −6 dB through the weld seam thickness is analysed using internally developed software, enabling a quantified evaluation. The proportion of pixels meeting the designated criterion is quantified and presented as a percentage in Table 3, denoted as the *OK Area* metric. The qualitative representation can be seen in the individual C-scan via the colour coding (Table 3) and is used to compare the homogeneity of the weld seams.

Due to individual settings on the ultrasonic flaw detector for each material, such as gates for the expected back wall echo of the sound signal, the used signal amplifications and the overall material thickness

(12 vs. 14 layers), a quantified comparison of the images and values can only be applied within the individual material examining the two process controllers. Therefore, considering the aforementioned boundary conditions, this method only allows a qualitative comparison between the different materials.

The weld seam can be qualitatively characterized and assessed through the chromatic scaling of the C-scan data, wherein the red extremity of the spectrum corresponds to optimal sonic transmission with minimal attenuation and scattering, whereas the blue extremity indicates elevated sound level attenuation associated with increased signal scattering. The gradational transition between these two extremes is visually represented by the continuum of colours within the spectrum. The images displayed in Table 3 orient the weld initiation on the left-hand side, indicating a weld progression direction from left to right, as also layout in Fig. 13.

A qualitative analysis of the images presented in Table 3 reveals that material #3 exhibits a markedly homogeneous chromatic gradient, with only sporadic localized regions of degraded quality (blue spots), whereas materials #1 and #2 are characterized by pronounced inhomogeneities. Notably, material #3 displays discrete anomalies in the scans obtained from both controllers, as exemplified by MAT03-AMP-No. 05, MAT03-POW-No. 01 and -No. 02 in Table 3.

Furthermore, the percentage area satisfying the −6 dB criterion is of comparable magnitude across both controllers, thereby precluding the identification of discernible differences between the two controllers for this particular material.

The visual inspection of the images corresponding to MAT01-POW, MAT01-AMP, and MAT02-POW reveals a tripartite segmentation. The initial weld seam region (left) exhibits a predominantly bluish-green shade, indicative of elevated signal attenuation and scattering, as evidenced by the low red content. This region is succeeded by a segment characterized by a preponderance of red colouration, which persists for approximately to the marker of 80% of the weld seam length. The terminal 20% of the weld seam is marked by a resurgence of inhomogeneous colouration, analogous to the start region. Notably, the intermediate segment, which is presumed to be associated with low sound signal attenuation, is situated within the time interval of approximately 1.5 to 15 s, corresponding to the weld seam length.

Furthermore, a comparative analysis across the materials reveals a notable disparity for material #02 between the amplitude-controlled and power-controlled welds. In contrast to materials #01 and #03,
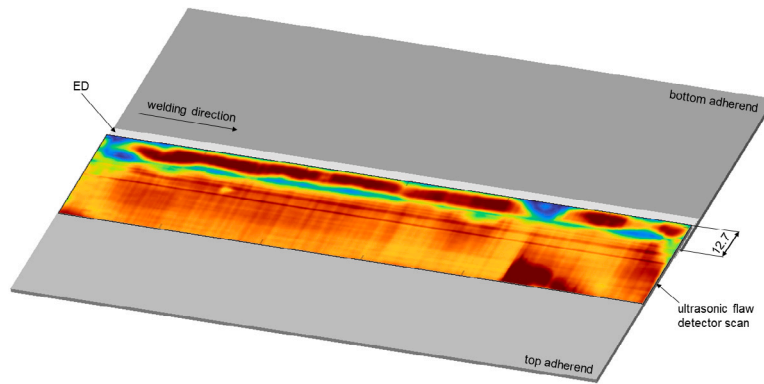
Fig. 13. Welded setup (top/bottom adherend & ED) showcasing an ultrasonic flaw detector C-scan.
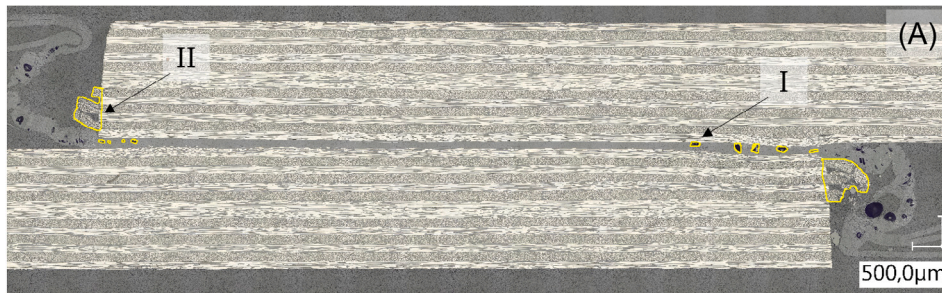

Fig. 14. Micrograph image of material #01, power-controller, weld number #05, section position #02, evaluation example (A) showcasing the porosity area (I) and fibre squeeze flow area (II).

which do not exhibit a discernible difference in weld quality between the two controllers, the amplitude-controller appears to yield a relatively inferior weld quality for material #02, suggesting a material-dependent variability in the controller's performance. Notwithstanding the initial weld seam of the amplitude-controller exhibiting a comparable quality to that of the power-controller, the subsequent weld seams (2nd–5th) demonstrate a marked decline in quality, as evidenced by the correlation between impaired sound transmission and elevated attenuation, which is assumed to be indicative of inferior weld seam quality.

A further examination of the ultrasonic flaw detection is conducted and interpreted in the context of the comprehensive findings of this study, as presented in Section 7.

6.2. Micrographic evaluation

A *VHX-5000* digital microscope from *Keyence*® is utilized in combination with a *VH-Z250R* lens to take the micrographs. The lens offers a magnification of between 250x and 2500x. Hence, panoramic views with a magnification of 250x are created and displayed with a scale of 500 μm, see Figs. 14–16. Each image shows the welded laminates in their overlap configuration (12.7 mm) with a rich matrix layer in between. In the left top and right bottom corner the squeezed out ED can be recognized, originated by the three individual films as described in Section 3.1. Enclosed by this study a quantified evaluation of the micrographs is provided by Table 4, estimating five different criteria, such as the porosity area [mm^2] (I), the area of squeezed out fibres [mm^2] (II) as shown in Fig. 14, the area of delamination [mm^2] (III), Fig. 15 as well as the displacement measurements [mm] at the left hand (V) and right hand (IV) end of the weld section as showcased in Fig. 16. The setting distance is quantified by measuring the residual total thickness of the welded components, comprising the pure matrix by subsequently subtracting the initial plate thickness from this value. The theoretical setting distance is presented in an inverted manner as the remaining pure matrix thickness in Table 4.

While criteria (I), (II) and (III) do not exhibit a statistically significant correlation with σ_{LSS} or any other evaluation criterion, at least with the data available, they may still provide insight into the underlying factors contributing to anomalous strength values in specific samples, thereby facilitating a more nuanced understanding of the observed variability in mechanical properties.

Notwithstanding the absence of a correlation with other criteria, a robust statistical relationship is observed between the residual matrix thickness, respectively the setting distance or displacement, and σ_{LSS}, which is subjected to further analysis and elucidation in the present study, with the corresponding data presented in Fig. 17.

This figure presents the mean strength values $\overline{\sigma}_{LSS}$ obtained from samples #01, #03, #05, #08, and #09 of the first four welds, with corresponding micrographs acquired from the fifth weld seam for recording the remaining matrix thickness measurements. The spatial locations of the samples were strategically selected based on a comprehensive analysis of the process data (Figs. 3–8), with the objective of interrogating regions of interest within the weld seam that exhibit unique characteristics or anomalies.
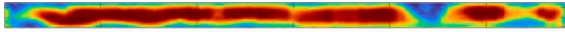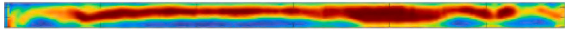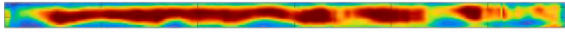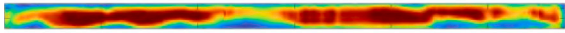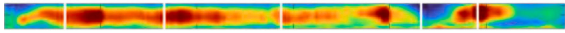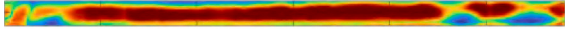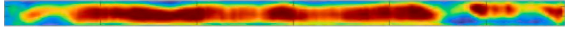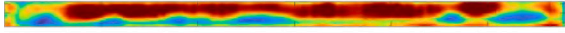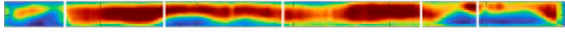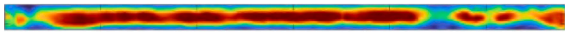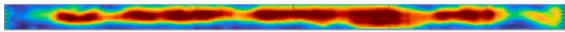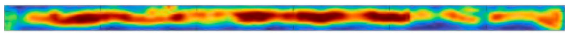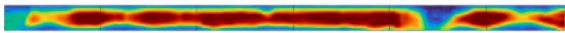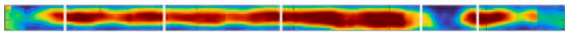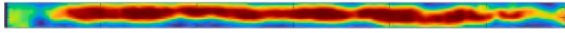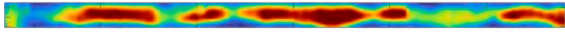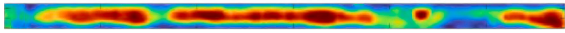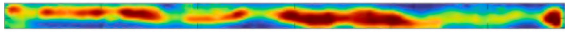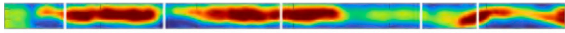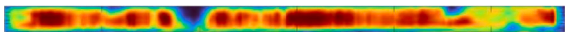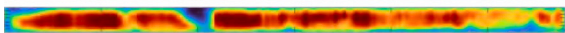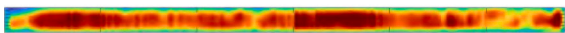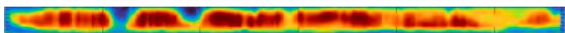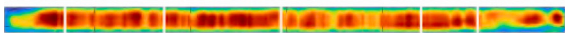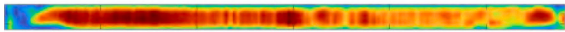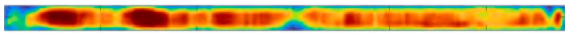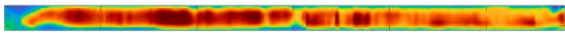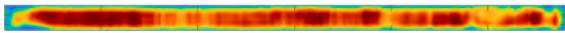
The residual pure matrix thickness was quantified by calculating the mean value along the weld seam depth, utilizing the data points from regions (IV) and (V) for the averaging process. The setting distance or displacement of the sonotrode is computed by subtracting the residual matrix thickness from the nominal energy director thickness of 300 mm, thereby yielding a quantifiable measure of the differential thickness, as shown in Fig. 17. Furthermore, the data is stratified by material type and controller configuration, with individual results displayed for each of the three materials and two distinct control systems, as illustrated in Fig. 17.

Although the individual data points from the different controllers exhibit a homogeneous distribution, a distinct material-dependent clustering pattern is evident, with the three materials forming separate groups.

Among the materials tested, Material #02 had the lowest LSS, which corresponded to the shortest setting distance. In contrast, Material #01

Table 3
Evaluation of the Ultrasonic Flaw Detector Scans - micrograph positions illustrated as white line markers in each weld No. 05.

Image	Material [-]	Controller POW/AMP	Weld No. [-]	OK Area [%]
	MAT01	POW	No.01	63.53
	MAT01	POW	No.02	57.51
	MAT01	POW	No.03	61.32
	MAT01	POW	No.04	62.86
	MAT01	POW	No.05	53.84
	MAT01	AMP	No.01	72.65
	MAT01	AMP	No.02	65.46
	MAT01	AMP	No.03	61.69
	MAT01	AMP	No.04	73.17
	MAT01	AMP	No.05	60.84
	MAT02	POW	No.01	50.91
	MAT02	POW	No.02	48.83
	MAT02	POW	No.03	43.74
	MAT02	POW	No.04	55.48
	MAT02	POW	No.05	49.27
	MAT02	AMP	No.01	53.89
	MAT02	AMP	No.02	42.86
	MAT02	AMP	No.03	40.24
	MAT02	AMP	No.04	42.81
	MAT02	AMP	No.05	41.81
	MAT03	POW	No.01	64.90
	MAT03	POW	No.02	66.94
	MAT03	POW	No.03	73.07
	MAT03	POW	No.04	66.93
	MAT03	POW	No.05	68.26
	MAT03	AMP	No.01	67.93
	MAT03	AMP	No.02	67.15
	MAT03	AMP	No.03	70.38
	MAT03	AMP	No.04	70.81
	MAT03	AMP	No.05	63.75
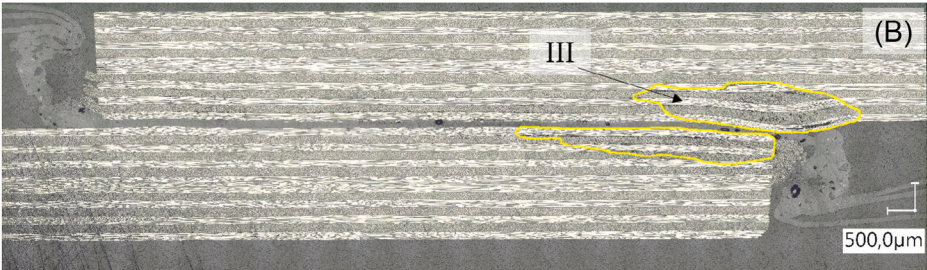
Fig. 15. Micrograph image of material #01, amplitude-controller, weld number #05, section position #05, evaluation example (B) showcasing the delamination area (III).

Fig. 16. Micrograph image of material #03, power-controller, weld number #05, section position #03, evaluation example (C) showcasing the displacement measurement position (IV) and (V).

Fig. 17. LSS values in relation to consolidation displacement.

showed the most consistent setting distance and had tensile strength values that fell within a higher range, although these values varied by as much as 20 MPa. Material #03 had the greatest setting distance and also exhibited the highest average tensile strength. A statistical analysis using the *Pearson* [41] method revealed a strong correlation between these two properties, evident by a correlation value r of 0.79 [42–44].

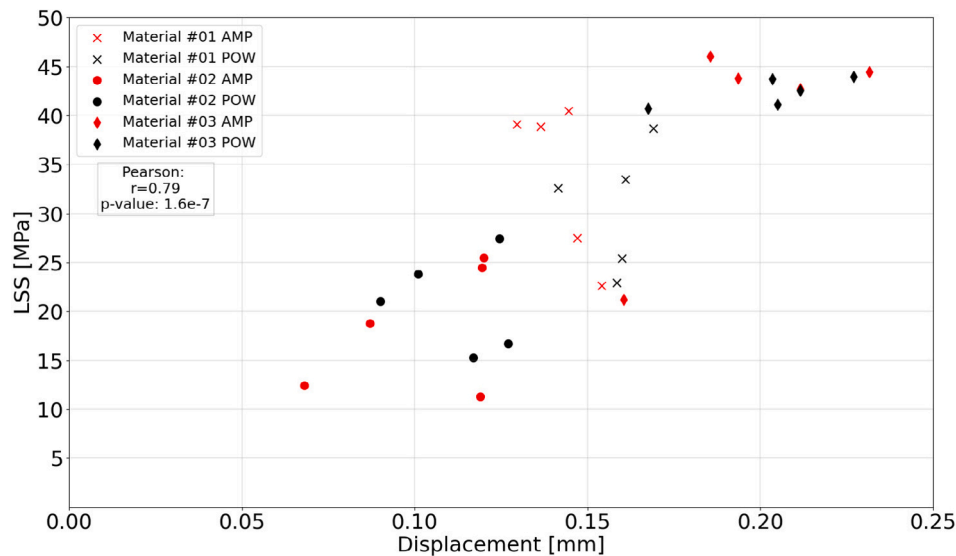Furthermore, the highly significant *p-value* (see Fig. 17) suggests that the observed effect is statistically significant ($p < 0.05$) [42]. However, it is essential to interpret this result with caution due to the limited sample size, which may impact the reliability and generalizability of the findings [41].

The correlation between setting distance and LSS reported herein is contextualized within the broader framework of the study's findings, and a more in-depth discussion of its implications is presented in Section 7.

6.3. Fracture surface analysis

Supplementing the primary and secondary analyses, a tertiary evaluation of weld quality is presented through a fractographic examination of representative weld specimens, with the resultant fracture surfaces displayed and annotated in Figs. 18–20. Each figure illustrates the bottom adherend of a distinct SLS sample for both control systems, with panels [A], [B], and [C] displaying the fracture surfaces of the amplitude-controlled welds, and panels [D], [E], and [F] presenting the corresponding power-controlled welds for comparative analysis. The three illustrations depict the various materials in chronological sequence, with the third weld seam of each material selected for analysis. A tripartite representation of fracture surfaces is presented for each material, comprising the initial (sample #01), central (sample

#05), and terminal (sample #09) regions of the weld seam. This allows for a comparative evaluation of the LSS at distinct stages of the welding process, with reference to the corresponding LSS values plotted in Figs. 10–12.

A detailed examination and side-by-side comparison of the three images reveals distinct variations in weld quality among the materials. Notably, the fracture surfaces of material #02 exhibit inferior bonding across all three samples, characterized by an elevated proportion of unmolten matrix (ED) and significant porosity. In contrast, material #01 displays a higher bond quality, exemplified by sample #05, which presents a homogeneous interlaminar fracture surface throughout the entire cross-sectional area, indicative of improved weld penetration and consolidation. Nevertheless, material #01 also exhibits a notable presence of unmolten matrix and corresponding porosity in samples #01 (C)(F) and #09 (A)(D), albeit to a lesser extent than observed in material #02, indicating a relatively improved weld quality despite some localized imperfections.

Fig. 20 illustrates the fracture surfaces of material #03, which exhibits the highest quality weld seams among the materials examined. A comparative analysis of sample #01 from material #03 with the corresponding samples from materials #01 and #02 reveals a notable distinction, as the bond in material #03 is consistently established throughout the entire cross-sectional area. This homogeneous bonding is a characteristic feature of the samples from material #03, including samples #05 and #09, which display a predominantly interlaminar fracture surface morphology, indicative of optimal weld quality and cohesive failure.

A thorough assessment of the fracture surfaces, isolated from material-specific effects and focusing on the control systems, reveals only subtle differences. However, a distinct disparity is evident in sample

Table 4
Micrograph Images Evaluation - (I): Area of porosity [mm²], (II): Area of squeezed out fibres [mm²], (III): Area of delamination [mm²], (IV): Displacement measurement, LH [mm], (V): Displacement measurement, RH [mm].

Material	Controller POW/AMP	Section No. [–]	(I) [mm²]	(II) [mm²]	(III) [mm²]	(IV) [mm]	(V) [mm]
MAT01	AMP	01	0.019	0.485	5.171	0.098	0.194
MAT01	AMP	02	0.001	0.056	0.000	0.150	0.177
MAT01	AMP	03	0.018	0.467	0.777	0.105	0.206
MAT01	AMP	04	0.001	0.106	0.096	0.154	0.187
MAT01	AMP	05	0.029	0.279	1.162	0.124	0.182
MAT01	POW	01	0.030	0.261	1.402	0.103	0.180
MAT01	POW	02	0.041	0.501	0.537	0.133	0.184
MAT01	POW	03	0.022	0.428	0.473	0.108	0.170
MAT01	POW	04	0.014	0.349	0.101	0.159	0.103
MAT01	POW	05	0.013	0.343	0.312	0.098	0.182
MAT02	AMP	01	0.264	0.908	5.919	0.154	0.208
MAT02	AMP	02	0.130	0.229	1.287	0.187	0.239
MAT02	AMP	03	0.090	0.722	1.091	0.168	0.193
MAT02	AMP	04	0.114	0.435	1.643	0.164	0.196
MAT02	AMP	05	0.023	0.033	0.121	0.212	0.252
MAT02	POW	01	0.306	0.757	6.417	0.147	0.199
MAT02	POW	02	0.131	0.838	4.271	0.180	0.240
MAT02	POW	03	0.075	1.012	1.734	0.141	0.257
MAT02	POW	04	0.023	0.922	0.309	0.164	0.187
MAT02	POW	05	0.190	0.477	2.012	0.154	0.212
MAT03	AMP	01	0.002	0.000	0.078	0.078	0.201
MAT03	AMP	02	0.002	0.000	0.060	0.060	0.117
MAT03	AMP	03	0.330	0.000	0.056	0.056	0.173
MAT03	AMP	04	0.001	0.000	0.073	0.073	0.140
MAT03	AMP	05	0.022	0.000	0.049	0.049	0.088
MAT03	POW	01	0.009	0.000	0.090	0.090	0.175
MAT03	POW	02	0.000	0.000	0.062	0.062	0.131
MAT03	POW	03	0.000	0.000	0.051	0.051	0.095
MAT03	POW	04	0.000	0.000	0.070	0.070	0.120
MAT03	POW	05	0.003	0.000	0.060	0.060	0.117
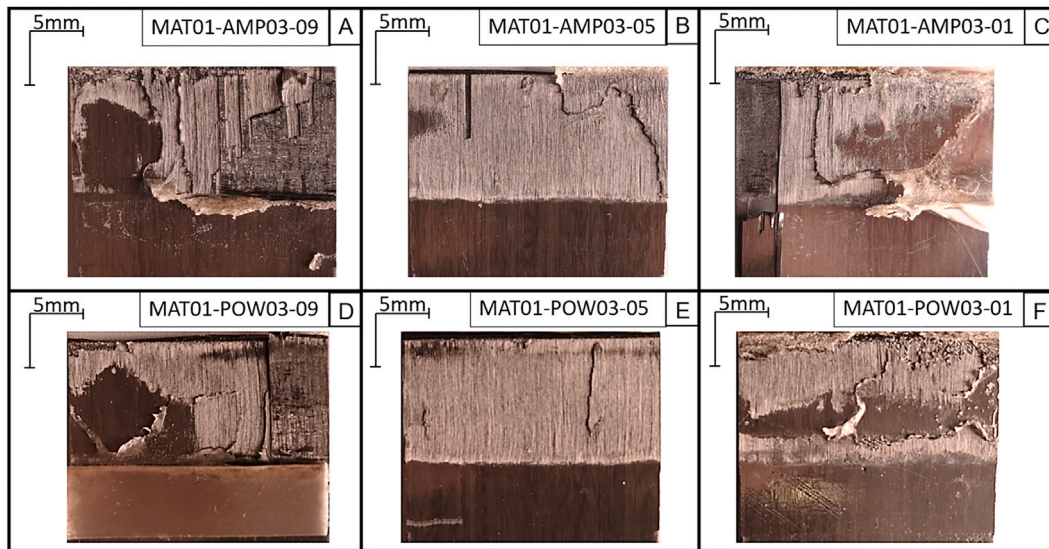
Fig. 18. Fracture surfaces of third weld seam of material #01, amplitude-controlled weld sample #09 (A), #05 (B), #01 (C), power-controlled weld sample #09 (D), #05 (E), #01 (F).

#01, where the amplitude-controller yields a higher proportion of unmolten matrix compared to the power-controller. This difference is particularly pronounced in materials #01 and #03, as illustrated in sections (C) and (F), suggesting a control system-dependent variation in weld quality, especially during the initial stages of the welding process.

A more in-depth examination and discussion of the aforementioned results can be found in Section 7, where the findings are further analysed and interpreted in greater detail.

7. Discussion

The study presented is prompted by the concept of maintaining a continuous energy equilibrium, wherein the input energy is balanced by the mechanical vibrational energy of the sonotrode and the dissipated energy, which is subsequently converted to thermal energy via damping mechanisms. By adopting this approach, it was hypothesized that a

Fig. 19. Fracture surfaces of third weld seam of material #02, amplitude-controlled weld sample #09 (A), #05 (B), #01 (C), power-controlled weld sample #09 (D), #05 (E), #01 (F).

Fig. 20. Fracture surfaces of third weld seam of material #03, amplitude-controlled weld sample #09 (A), #05 (B), #01 (C), power-controlled weld sample #09 (D), #05 (E), #01 (F).
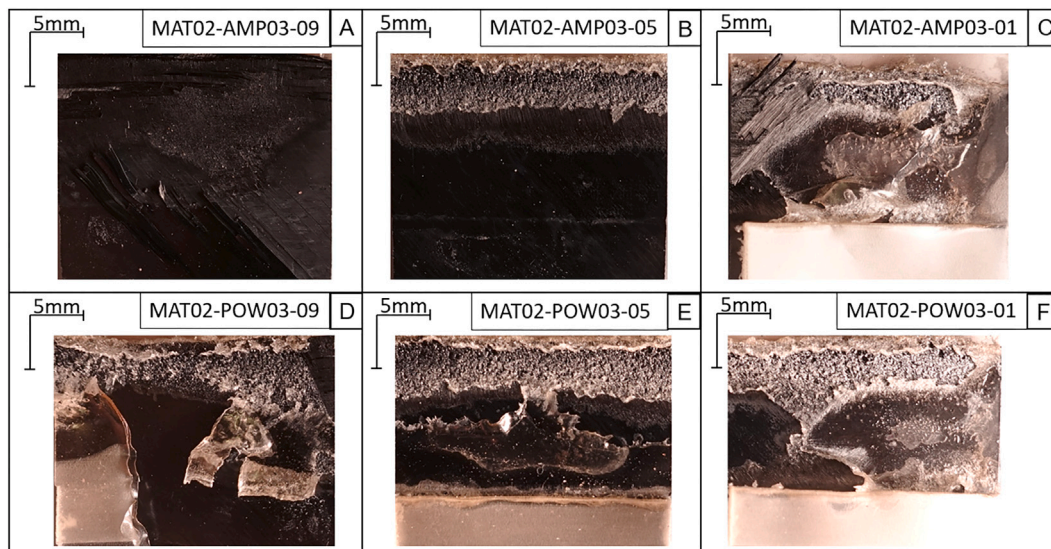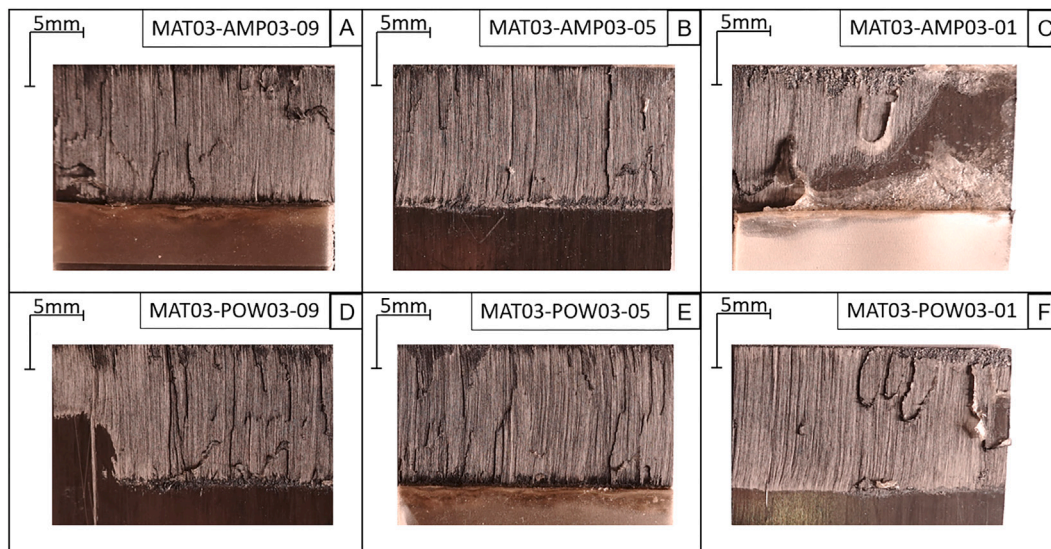
uniform welding outcome could be attained throughout the entire length of the weld seam.

As previously established by Villegas in the context of static ultrasonic welding, a strong correlation exists between the emitted power of the ultrasonic welding device, the trajectory of the sonotrode, and the resultant squeeze flow of the neat matrix material, which, in turn, directly influences the quality of the joint [18].

Villegas has delineated a five-stage paradigm for the static ultrasonic welding process, characterized by a constant amplitude, wherein each phase is distinguished by distinct attributes. The initial phase is marked by a high energy gradient, initiating the process through a boundary surface friction between the top and bottom adherend as well as the ED separating the welding partners. This initiating surface friction dominates the heat generation until the glass transition temperature is reached. Once the glass transition temperature is surpassed, the main contribution to the heat generation is provided through an intermolecular, viscoelastic friction. Both mechanisms heat up the bonding area until a certain peak in power is reached, corresponding to the processing temperature of the thermoplastic matrix and termination

of phase 1. Phases 2–4 are characterized by a progressive increase in thermal energy within the weld seam, accompanied by a gradual augmentation of the setting distance, resulting in a corresponding increment in the squeeze flow of the neat matrix material, the ED. The second phase marks the transition towards a flowing state of the neat resin matrix ED, commencing by a decreasing power and a nearly constant displacement of the sonotrode. The aforementioned phase is ceased by a local power minimum and an incremental increase of the sonotrode displacement [18]. Terminating the welding process within this phase, leads to partially non-molten and unbonded zones within the weld seam due to an unfavourable low energy dissipated through the ED. Consequently, phase 3 is entered. Phase 3 establishes a congruent behaviour of power and sonotrode displacement as both variables are increasing. Hence, a present and continuous squeeze flow of the thermoplastic pure matrix is descriptive for this phase, accompanied by a rapid increase of power [23]. Specimens welded until this stage exhibit an increased joint strength, provided by a completely molten ED across the weld seam cross section and proper consolidation during solidification [18]. Notably, Phase 4 is

distinguished by the attainment of an energy equilibrium, despite a continued increase in setting distance. The indicated equilibrium can be elucidated by the continuation of the squeeze flow, therefore a certain power consumption, while simultaneously distributing heat to the top and bottom adherends, leading to a reduced and counteracting power demand [18,23]. The process culminates in Phase 5, where the neat matrix material is entirely expelled from the joining zone, leading to an intimate contact between the joining partners. However, this terminal phase is also associated with an increased propensity for delamination and porosity, thereby underscoring the importance of terminating the welding process ideally within Phase 4 to optimize joint quality [18].

As anticipated, the experimental approach of maintaining consistent welding parameters across the three distinct materials (see Section 3.2), with the aim of elucidating the resultant effects on process data and weld seam quality, yielded divergent outcomes with respect to the phases delineated by Villegas, thereby illustrating material-specific differences in the ultrasonic welding process.

Although the phases of static ultrasonic welding cannot be directly extrapolated to continuous welding without modification, the authors hypothesize that the phases are present in a temporally extended manner, exhibiting analogous characteristics, thereby suggesting a scalable framework for understanding the continuous welding process.

Within the broader context of the study's findings, the authors infer that, irrespective of the controller employed, material #02 was situated in Phase 2, material #01 was in Phase 3, and material #03 was in Phase 4, suggesting a material-specific progression through the phases of the ultrasonic welding process.

This inference is substantiated by the fracture surface morphology of the various materials, as illustrated in Figs. 18–20. Notably, material #02 exhibits a higher proportion of unbonded matrix (Fig. 19), characteristic of a cold weld. In contrast, material #01 displays a homogeneous fracture surface, particularly in the central region of the weld (Fig. 18, sections B and E), suggesting a more advanced stage in the welding process. Furthermore, material #03 appears to have progressed even further in the welding phase, as evidenced by the fracture surfaces of individual samples (Fig. 20, sections D, E, and F), particularly in the case of power-controlled weld seams.

Additionally, the power curves obtained from the amplitude-controlled welds exhibit distinct behavioural patterns. Notably, the power curve for material #02 (Fig. 5) reveals a pronounced decrease in power over the time interval spanning from t=2 s to t=15 s, which is consistent with the characteristic power trend observed by Villegas for static welding in stage 2 [18].

Material #01 exhibits a metastable state of output power, characterized by a rapid attenuation of the initial peak, followed by a plateau-like regime with a moderate decline in power over the time interval spanning from t=2 s to t=15 s, indicating a relatively stable energy output, see Fig. 3. In contrast, material #03 exhibits a distinctly different temporal evolution of its power curves, as illustrated in Fig. 7. Outstandingly, the power output remains relatively constant, with a slight incremental increase over time, thereby corroborating the hypothesis that the three materials were situated in disparate phases of the welding process.

The hypothesis can be further substantiated by the micrograph findings and the analysis of the setting path and matrix squeeze flow. As illustrated in Fig. 17, a robust linear correlation is observed between the setting path, respectively the displacement and the tensile strength of the weld samples, which is consistent with the previously discussed power curves. A high displacement of the consolidated weld seam necessitates a correspondingly favourable and elevated temperature of the ED, thereby facilitating the squeeze flow, as evidenced by the data points of material #03, which exhibit high LSS values concomitant with a high setting path. In contrast, material #02, having undergone a low setting path, has likely experienced insufficient energy and temperature, resulting in inferior quality and low LSS values. The intermediate phase is exemplified by material #01, which displays

moderate LSS values and a medium setting distance, suggesting that the matrix flow has occurred, albeit with a suboptimal ratio of temperature and pressure.

Ultimately, the distinct welding stages of the various materials can be discerned in the flaw detection scans, as shown in Table 3, with the qualitative disparity being most pronounced for material #03. Principally, materials #01 and #02 yield water-coupled ultrasound images characterized by various defects, whereas material #03 exhibits a remarkably homogeneous weld quality along the entire weld seam, with only minor, stochastic variations being apparent.

A subsequent step involves conducting a comparative analysis of the two controllers to elucidate their distinct characteristics. A key observation can be made in this regard: the power-controller exhibits greater agility, albeit at the expense of increased sensitivity, whereas the amplitude-controller demonstrates enhanced robustness, albeit with a concomitant decrease in responsiveness.

The enhanced agility of the power-controller is exemplified by material #03, as evident from the LSS values and fracture surfaces of sample #01. In particular, the min to max range of the first sample produced by the amplitude-controller is approximately 50% of the residual weld seam strength, whereas no discernible reduction in strength is observed in the initial region of the weld seam produced by the power-controller, see Fig. 12. Furthermore, the diminished connection quality of sample #01 from the amplitude-controller is also apparent in the fracture surfaces, as illustrated in Fig. 20, section (C). In contrast, the fracture surface of sample #01 (F) of the power-controller, is characterized by a higher proportion of welded matrix, underscoring the superior performance of the power-controller in this regard.

This phenomenon is less pronounced for material #02, which was situated in a distinct phase of the welding process, and only marginally evident for material #01. Nevertheless, the superior agility of the power-controller is exemplified at another juncture in the welding progression. Upon analysing the LSS values of materials #01 and #02, a notable decline is observed between samples #08, #09, and #10 for both controllers, which the authors attribute to the spot clamping mechanism illustrated in Fig. 1. The power-controller demonstrates a greater capacity for restoring the weld quality after the decline at sample #09, compared to the amplitude-controller. This is particularly apparent in the case of material #02, where the LSS mean values of the power-controlled welds at samples #08 and #10 are commensurate, whereas the amplitude-controlled sample at point #10 yields even lower values than the preceding sample #08, underscoring the relative merits of the power-controller in this context.

In contrast to the power-controller, which exhibits a highly agile yet sensitive response, the amplitude-controller demonstrates a robust and stable behaviour, thereby offering a distinct advantage in terms of reliability and consistency. This phenomenon is particularly pronounced in material #03, see Fig. 12, where the min to max range of the individual sample LSS values for the analysed weld seams exhibits a correspondingly low variability. However, exceptions to this trend are observed in samples #01, #03, and #10, which correspond to the initiation of the weld seam and the clamping mechanism, as shown in Fig. 1. These samples are characterized by increased scatter, suggesting that a more rapid response, such as that afforded by the power-controller, is necessary to mitigate these variations and maintain a consistent weld quality. Additionally, the metastable state of material #01 suggests that initializing the weld seam with a high energy input can be advantageous, as demonstrated in Fig. 10 and the power curves in Fig. 3. A remarkable disparity is observed between the amplitude and power-controllers for material #01. The amplitude-controller achieves a robust plateau with high LSS values between the second and eighth samples, whereas the power-controller exhibits a gradual increase with significant scatter. This discrepancy is attributed to the high energy input of the amplitude-controller, which reaches approximately 1750 W after t=1.5 s, as shown in Fig. 7. In contrast, the power-controller rapidly attains saturation of its maximum output amplitude within the

first few seconds, resulting in limited energy transfer during this period and ultimately leading to a suboptimal viscoelastic equilibrium, which compromises the overall quality of the weld seam. This highlights a distinct benefit of the amplitude-controller, which is not inherently constrained by the maximum continuous output power of the end device, rated at 2000 W, thereby allowing for more flexible and efficient energy delivery. One potential strategy to mitigate the saturation of the amplitude during power-controlled welding is to incrementally increase the welding force applied by the sonotrode [18].

Provided that the operational parameters fall within an opportune process window, analogous to that observed with material #03, the power controller exhibits a distinct benefit. This exceptional asset of the power-controller is its ability to maintain a remarkably low standard deviation of LSS values within a weld, consistently below 10%, as evidenced in Table 2, highlighted in blue for material #03. In contrast, the amplitude-controller exhibits a substantially higher standard deviation, approximately twice that of the power-controller, which is largely attributable to the variability introduced by sample #01 of the individual weld seam. In contrast, when process parameters deviate from ideal conditions and an unstable or metastable process prevails, the robust behaviour of the amplitude controller becomes advantageous. An examination of Figs. 10 and 11, corresponding to phase 2 and 3 of the welding process, respectively, reveals that the agility of the power controller exhibits drawbacks, as evidenced by a higher sample standard deviation Fig. 10 and increased standard deviation across individual weld seams (Table 2) during non-optimal welding processes. Conversely, the amplitude controller yields a robust outcome in weld quality, even in metastable process conditions, as demonstrated by the LSS values in Fig. 10. However, if the total energy input is insufficient, an amplitude-controlled weld seam exhibits a comparable magnitude of variability to a power-controlled one, as illustrated in Fig. 11 for material #02.

Therefore, the advantages of both controllers are believed to be key elements of a future cascaded control architecture to proficiently master complex three-dimensional weld seam geometries. It is hypothesized by the authors that the requirement for an adaptable control architecture stems from the presence of complexities such as discrete thickness variations in the adherends, arising from optimized layer stacking of individual components, and boundary constraints, including the clamping of the parts to be welded.

8. Conclusion and outlook

The presented study introduces a novel approach to process control for continuous ultrasonic welding of fibre-reinforced, thermoplastic high-performance polymers. Through experimentation with diverse materials, it is demonstrated that equivalent weld seam quality can be attained using constant power-control, comparable to the current state-of-the-art amplitude-control method. Above all, only minor discrepancies are observed, such as variations in maximum LSS values, which can be mitigated through individual optimization. The primary outcome of this research is the identification of the power-controller's agile behaviour, enabling more rapid compensation for deviations along the weld seam, whereas the amplitude-controller exhibits greater robustness, albeit at the expense of responsiveness.

Additional research is required to elucidate the correlation between amplitude and power as a function of laminate stacking and proportional ED thickness, with the ultimate goal of refining the process window for the respective controller to enhance precision, accuracy and reproducibility.

As a medium-term outlook, the authors see the potential to investigate further control methods that regulate the process in a comparable manner with similar weld quality. The welding speed and the sonotrode force can be mentioned as possible parameters. The optimized controller architecture for the continuous ultrasonic welding process can be further enhanced by incorporating cascaded structures, thereby leveraging the distinct benefits of each control method to yield a consistently homogeneous welding result with high reproducibility.

CRediT authorship contribution statement

Maximilian Janek: Writing – review & editing, Writing – original draft, Validation, Supervision, Methodology, Investigation, Formal analysis, Data curation, Conceptualization. **Dominik Görick:** Writing – review & editing, Investigation, Conceptualization. **Lars Larsen:** Writing – review & editing, Writing – original draft, Investigation, Conceptualization. **Stefan Jarka:** Writing – review & editing, Investigation. **Michael Kupke:** Writing – review & editing.

Declaration of competing interest

The authors declare that they have no known competing financial interests or personal relationships that could have appeared to influence the work reported in this paper.

Acknowledgment

Data availability

Data will be made available on request.

References

[1] Larsen Lars, Endrass Manuel, Jarka Stefan, Bauer Simon, Janek Maximilian. Exploring ultrasonic and resistance welding for thermoplastic composite structures: Process development and application potential. Compos Part B: Eng 2025;289:111927.

[2] Barile Marco, Lecce Leonardo, Iannone Michele, Pappadà Silvio, Roberti Pierluca. Thermoplastic composites for aerospace applications. In: Revolutionizing aircraft materials and processes. Springer International Publishing; 2020, p. 87–114.

[3] Jarka Stefan, Endraß Manuel, Engelschall Manuel, Bauer Simon. Fügetechnologien in der luftfahrt - Besondere anforderungen an die schweiß prozesse joining technologies in aviation - particular requirements for the welding processes. Join Plast - Fügen Von Kunststoffen 2019;(1):47–53.

[4] Gardiner Ginger. Thermoplastic composite demonstrators — EU roadmap for future airframes. 2018, https://www.compositesworld.com/articles/thermoplastic-composite-demonstrators-eu-roadmap-for-future-airframes-. [Accessed 18 April 2024].

[5] Black Sarah. Thermoplastic composites "clip" time, labor on small but crucial parts. 2015, https://www.compositesworld.com/articles/thermoplastic-composites-clip-time-labor-on-small-but-crucial-parts. [Accessed 18 April 2024].

[6] B. G. Brito C, Teuwen J, Dransfeld CA, F. Villegas I. The effects of misaligned adherends on static ultrasonic welding of thermoplastic composites. Compos Part A: Appl Sci Manuf 2022;155:106810.

[7] Villegas Irene Fernandez. Strength development versus process data in ultrasonic welding of thermoplastic composites with flat energy directors and its application to the definition of optimum processing parameters. Compos Part A: Appl Sci Manuf 2014;65:27–37.

[8] Villegas Irene Fernandez, Palardy Genevieve. Ultrasonic welding of CF/PPS composites with integrated triangular energy directors: melting, flow and weld strength development. Compos Interfaces 2016;24(5):515–28.

[9] Zhao Tian, Broek Charlotte, Palardy Genevieve, Villegas Irene Fernandez, Benedictus Rinze. Towards robust sequential ultrasonic spot welding of thermoplastic composites: Welding process control strategy for consistent weld quality. Compos Part A: Appl Sci Manuf 2018;109:355–67.

[10] Engelschall M, Larsen L, Fischer F, Kupke M. Robot-based contiuous ultrasonic welding for automated production of aerospace structures. In: society for the advancement of material and process engineering. SAMPE; 2019.

[11] Engelschall M, Jarka S, Fischer F, Willmeroth M, Larsen L. Development of continuous ultrasonic welding for the automated production of aircraft primary structures. In: ITHEC 2018. ITHEC 2018 Messe Bremen; 2018.

[12] Roth York C, Herrmann Ralf, Sanchez Santos Cristina, Uellendahl Matthias, Koopman Joost, Henneberg Andreas, Kos Johan, et al. Cleansky2/ clean aviation large passenger aircraft for more sustainable commercial fuselage technologies – major achievements. In: International council of the aeronautical sciences. 2023.

[13] Köhler Filipp, Fernandez Villegas Irene, Dransfeld Clemens, Herrmann Axel. On the influence of welding parameters and their interdependence during robotic continuous ultrasonic welding of carbon fibre reinforced thermoplastics. Materials 2024;17(21):5282.

[14] Jongbloed Bram, Teuwen Julie JE, Villegas Irene Fernandez, Benedictus Rinze. Investigation on the melting of the weld interface in continuous ultrasonic welding of thermoplastic composites. In: 22nd International Conference on Composite Materials, vol. 22nd, Melbourne, Australia: ICCM 2019; 2019.

[15] Jongbloed Bram, Teuwen Julie, Villegas Irene Fernandez. On the use of a rounded sonotrode for the welding of thermoplastic composites. J Adv Join Process 2023;7:100144.

[16] Jongbloed Bram, Teuwen Julie, Palardy Genevieve, Fernandez Villegas Irene, Benedictus Rinze. Continuous ultrasonic welding of thermoplastic composites: Enhancing the weld uniformity by changing the energy director. J Compos Mater 2019;54(15):2023–35.

[17] Brito CBG, Teuwen J, Dransfeld CA, Villegas IF. Ultrasonic welding of thermoplastic composites: A comparison between polyetheretherketone and low-melt polyaryletherketone as resin in the adherends and energy directors. Compos Part B: Eng 2025;296:112264.

[18] Villegas Irene Fernandez. In situ monitoring of ultrasonic welding of thermoplastic composites through power and displacement data. J Thermoplast Compos Mater 2013;28(1):66–85.

[19] B. G. Brito C, Teuwen J, Dransfeld CA, F. Villegas I. On improving process efficiency and weld quality in ultrasonic welding of misaligned thermoplastic composite adherends. Compos Struct 2023;304:116342.

[20] Brandt L, Vistein M, Deden D, Gänswürger P, Janek M, Larsen L, et al. Tool- and jigless production of thermoplastic CFRPS based on cooperating robots. In: SAMPE Europe conference 2024 Belfast. 2024.

[21] Benatar Avraham, Cheng Zhang. Ultrasonic welding of thermoplastics in the far-field. Polym Eng Sci 1989;29(23):1699–704.

[22] Benatar Avraham, Eswaran Raman V, Nayar Satinder K. Ultrasonic welding of thermoplastics in the near-field. Polym Eng Sci 1989;29(23):1689–98.

[23] Benatar Avraham, Gutowski Timothy G. Ultrasonic welding of PEEK graphite APC-2 composites. Polym Eng Sci 1989;29.

[24] Tsiangou Eirini, Teixeira de Freitas Sofia, Villegas Irene Fernandez, Benedictus Rinze. Ultrasonic welding of epoxy- to polyetheretherketone- based composites: Investigation on the material of the energy director and the thickness of the coupling layer. J Compos Mater 2020;54(22):3081–98.

[25] Lee Tae Hwa, Fan Hua-Tzu, Li Yang, Shriver Daniel, Arinez Jorge, Xiao Guoxian, et al. Enhanced performance of ultrasonic welding of short carbon fiber polymer composites through control of morphological parameters. J Manuf Sci Eng 2019;142(1).

[26] Jongbloed Bram, Teuwen Julie, Benedictus Rinze, Villegas Irene Fernandez. On differences and similarities between static and continuous ultrasonic welding of thermoplastic composites. Compos Part B: Eng 2020;203:108466.

[27] Ahanpanjeh M, Koehler F, Adomat V, Kober C, Fette M, Wulfsberg J. Impact of alignment of the sonotrode on the quality of thermoplastic composite joints in continuous ultrasonic welding. In: SAMPE Europe conference 2022 Hamburg. 2022.

[28] Ahanpanjeh Maryam, Fette Marc, Wulfsberg Jens P. Contribution of process parameters to geometric deviations of the robot for continuous ultrasonic welding process of thermoplastic composites. In: 2023 28th international conference on automation and computing. IEEE; 2023, p. 1–7.

[29] Bu Yin, Liao Wenhe, Tian Wei, Zhang Jin, Zhang Lin. Stiffness analysis and optimization in robotic drilling application. Precis Eng 2017;49:388–400.

[30] Branson Ultrasonics Corp. DCX S Power supply - Operating manual. Boorkfield, Connecticut, USA: Branson; 2025, https://www.emerson.com/documents/automation/operator-manual-4000839-dcx-s-power-supply-en-5260226.pdf. [Accessed 17 February 2025]. Document ID: 4000839, Revision 02.

[31] Lee Jun-Ho, Lee Hwa-Chun, Choi Jun-Ho, Park Sung-Jun, Nam Hae-Gon. 10Kw industrial ultrasonic welder design. In: INTELEC 2009 - 31st international telecommunications energy conference. IEEE; 2009, p. 1–6.

[32] Volosencu C. Control system for ultrasonic welding devices. In: 2008 IEEE international conference on automation, quality and testing, robotics. IEEE; 2008, p. 135–40.

[33] Toray. Toray cetex TC1225 product description. 2025, https://www.toraytac.com/product-explorer/products/gXuK/Toray-Cetex-TC1225. [Accessed 18 March 2025].

[34] Villegas IF, Grande BV, Bersee HEN, Benedictus R. A comparative evaluation between flat and traditional energy directors for ultrasonic welding of thermoplastic composites. In: 16th European conference on composite materials. Seville, Spain: ECCM16; 2014.

[35] Tsiangou E, Teixeira de Freitas S, Fernandez Villegas I, Benedictus R. Ultrasonic welding of CF/Epoxy to CF/PEEK composites: Effect of the energy director material on the welding process. In: 18th European conference on composite materials. Athens, Greece: ECCM18; 2018.

[36] Tsiangou Eirini, Teixeira de Freitas Sofia, Fernandez Villegas Irene, Benedictus Rinze. Investigation on energy director-less ultrasonic welding of polyetherimide (PEI)- to epoxy-based composites. Compos Part B: Eng 2019;173:107014.

[37] Villegas Irene Fernandez. Ultrasonic welding of thermoplastic composites. Front Mater 2019;6.

[38] Bhudolia Somen K, Gohel Goram, Leong Kah Fai, Islam Aminul. Advances in ultrasonic welding of thermoplastic composites: A review. Materials 2020;13(6):1284.

[39] Görick Dominik, Larsen Lars, Engelschall Engelschall, Schuster Alfons. Quality prediction of continuous ultrasonic welded seams of high- performance thermoplastic composites by means of artificial intelligence. Procedia Manuf 2021.

[40] Endrass M, Thomé A, Gadletz V, Bauer S, Jarka S, Gänswürger P, et al. Resistance welding of low-melt polyaryletherketone: Process definition and optimization. In: 20th European conference on composite materials. Lausanne, Switzerland: ECCM20; 2022.

[41] Virtanen Pauli, Gommers Ralf, Oliphant Travis E, Haberland Matt, Reddy Tyler, Cournapeau David, et al. Scipy 1.0: Fundamental algorithms for scientific computing in python. Nature Methods 2020;17:261–72.

[42] Boslaugh Sarah. Statistics in a nutshell. Sebastopol, Calif.: O'Reilly Media; 2008, Title from title screen. - Includes index,

[43] Schober Patrick, Boer Christa, Schwarte Lothar A. Correlation coefficients: Appropriate use and interpretation. Anesthesia Analg 2018;126(5):1763–8.

[44] Akoglu Haldun. User's guide to correlation coefficients. Turk J Emerg Med 2018;18(3):91–3.